LASER & PHOTONICS REVIEWS

www.lpr-journal.org

Optical Phase Contrast Microscopy with Incoherent Vortex Phase

*Mengting Zhao, Xinzhou Liang, Jiasui Li, Mengyuan Xie, Huadan Zheng, Yongchun Zhong, Jianhui Yu, Jun Zhang, Zhe Chen, and Wenguo Zhu**

A novel, compact, and broadband optical phase contrast microscopy based on incoherent vortex topological quadrupole is theoretically proposed and experimentally realized. The topological quadrupole, generated in a thin uniaxial crystal, possesses four single-charge optical vortexes, each of which can act as a two-dimensional (2D) optical spatial differentiator. The incoherence of light-emitting diode (LED) light will wash out the optical vortex and the spatial differentiation effect, which can be ingeniously overcome by choosing Kohler illumination and inserting a 1 mm-thickness uniaxial crystal sandwiched with two polarizers before the camera. By adjusting the polarizers and the tilted angle of crystal to selectively utilize the geometric Berry phase and the angular gradient of Fresnel transmission coefficients of crystal, the 1D, 2D, and second-order analog spatial differentiations with a spatial resolution better than 0.775 μm can be switched flexibly. A versatile phase contrast microscope is built, which is well compatible with the conventional microscopes. The uniformly incoherent illumination without laser speckle effects results in high-quality spatial differentiation imaging. Biologically transparent living cells are thus imaged with high contrast.

1. Introduction

Fast and reliable detection and recognition of an object via light wave is the fundamental key to optical imaging, machine learning, and artificial intelligence. Optical phase contrast imaging, allowing us to realize not only the edge enhancement for amplitude patterns but also the conversion of non-visible phase patterns to intensity information, is one of the most effective way for the objective detection and recognition, thus has been widely used in biological imaging and optical analog computing.[1–6] Different kinds of optical phase contrast imaging have been proposed including Zernike phase-contrast,[7] Nomarski differential interference contrast,[8] and spiral phase contrast imaging,[9–12] as well as optical spatial differentiation. Among these imaging methods, the recently demonstrated optical spatial differentiation shows great advantages owing to its two-dimensional (2D) isotropic edge-enhancement, relatively compact optical configuration,[13] and broad operation band ranging from the visible to the mid-infrared.[2–15]

Optical spatial differentiation is one of the optical analog signal processing technologies, which is high-speed and low-power consumption with respect to its digital counterparts. In 2017, Zhu et. al demonstrated a 1D spatial differentiation associated with the surface plasmon excitations at a single metal–dielectric interface.[16] They illuminated obliquely a p-polarized beam on the metal surface from the glass side to excite surface plasmon. The reflected light field emerged as the first-order derivative of the illuminated light field.[16] By establishing a connection between optical spatial differentiation and a non-trivial topological charge in the optical transfer function, 2D spatial differentiation has been experimentally demonstrated on a single unpatterned interface under total internal reflection or partial reflection near-Brewster incidence.[17,18] However, the reflection configuration does not appeal to the optical microscope.

Recently, Pancharatnam Berry (PB) phase metasurfaces have been demonstrated for the 1D and 2D spatial differentiations.[19–21] The metasurface can introduce a PB phase gradient at the Fourier plane, resulting in the spatial separation of the right and left circular polarization (RCP and LCP) images. When the spatial separation is much smaller than the image profile, the outputted light field after a polarizer is approximately proportional to the first-order derivative of the input field. In 2021, Zhou and co-workers demonstrated a broadband 2D spatial differentiation and high-contrast edge imaging with a dielectric PB metasurface.[20] They demonstrated further that a polarization-entangled photon source can be used to switch ON or OFF the optical edge detection mode.[4] In addition to the PB metasurfaces, Fan' group realized a Laplacian for image

M. Zhao, X. Liang, J. Li, M. Xie, H. Zheng, J. Zhang, Z. Chen, W. Zhu
Key Laboratory of Optoelectronic Information and Sensing Technologies of Guangdong Higher Education Institutes
Department of Optoelectronic Engineering
Jinan University
Guangzhou 510632, China
E-mail: zhuwg88@163.com

Y. Zhong, J. Yu
Guangdong Provincial Key Laboratory of Optical Fiber Sensing and Communications
Jinan University
Guangzhou 510632, China

The ORCID identification number(s) for the author(s) of this article can be found under https://doi.org/10.1002/lpor.202200230

DOI: 10.1002/lpor.202200230

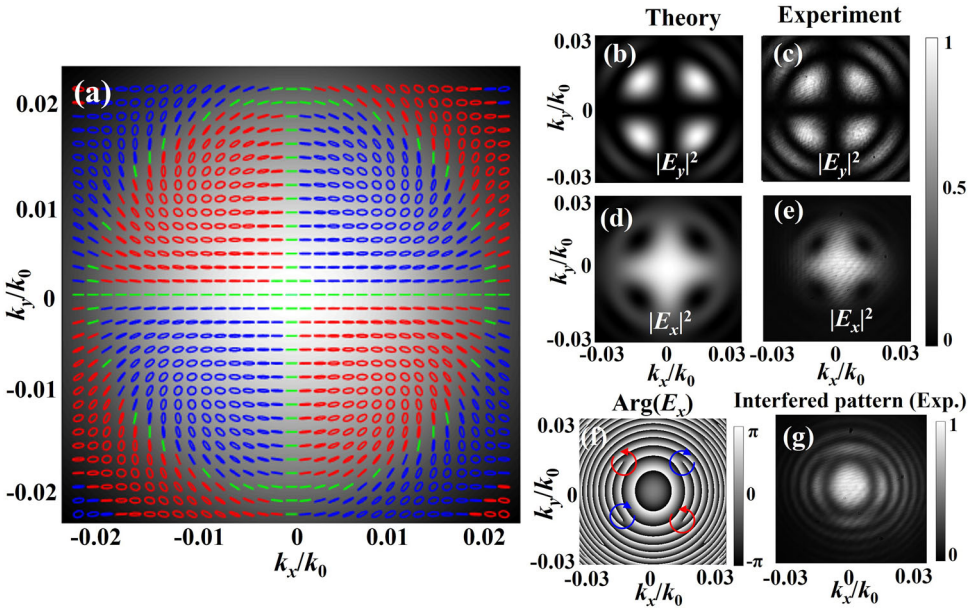

Figure 1. a) Momentum–space distributions of intensity and polarization states of light field outputted from a YVO4 crystal, where the blue, red, and green lines represent the right, left elliptical, and linear polarization states, respectively. b–e) Intensity distributions for the y- and x-components of outputted field. f) The phase distribution of the x-component of light field and g) the measured interfered intensity pattern between the x-component and a plane wave unveil the four optical vortexes with ±1 topologic charges.

differentiation using the guided resonances in a photonic crystal slab.[22] In 2020, Zhou et al. experimentally demonstrated a 2D spatial differentiator consisting of a Si nanorod photonic crystal.[13] However, these nanostructure devices are difficult in fabrications and coherent illuminations are used in the spatial differentiations.

Differently, here a novel, low-cost, and compact optical phase-contrast microscope is built by simply inserting a thin uniaxial crystal, sandwiched with two polarizers, into a conventional microscope. The bright field, 1D, 2D, and second-order spatial differentiation imaging can be flexibly switched by adjusting the polarizers and the tilted angle of crystal to selectively utilize the geometric Berry phase and the angular dispersion of the transmission coefficients of uniaxial crystal. With the light-emitting diode (LED) illuminating light, analog computing with incoherent light is achieved, and high-quality spatial differentiation imaging for undyed onion epidermal cells and NIH-3T3 living cells is demonstrated.

2. Spatial Differentiation with a Uniaxial Crystal

Assume a paraxial light beam transmitting through a uniaxial crystal with its optical axis perpendicular to the input interface. The incident beam can be considered as a superposition of plane waves with different wavevectors. For each wavevector, there are p and s waves, which change with the transverse wavevector $k_{x,y}$, since the local incident planes are determined by the local wavevector and normal vector of the interface.[23] If the incident beam is Gaussian beam incident normally into the uniaxial crystal, the p and s (extraordinary and ordinary) waves are respectively the radial and azimuthal polarization states, which propagate independently within the crystal. Thus, for a horizontally linear incident polarization, the transmitted light field from crystal possesses complex polarization distribution, containing C points and L lines (see **Figure 1**a). When decomposing the transmitted field into the x and y-polarized components, one finds that there are four main petals in the intensity pattern for the x-component in momentum–space (see Figure 1b,c). A vortex topologic quadrupole emerges in the y-component transmitted field,[25] as shown in Figure 1d–g. The vortex topologic quadrupole consists of four optical vortexes with ±1 topological charges, which are identified by the phase distribution of x-component and the interfered intensity pattern between the x-component and a plane wave (see Figure 1f,g). As will be demonstrated below, both the x- and y-components of the transmitted field can be employed for analog spatial differentiations.

In order to utilize the uniaxial crystal for spatial differentiation, a paraxial beam should be launched through a uniaxial crystal with a small incident angle. Based on the vectorial angular spectrum analysis method, the uniaxial crystal can be described by a transformation matrix, which connects the transmitted and incident angular spectrum. According to Ref. [23], the transformation matrix is in form of

$$\hat{T} = \begin{bmatrix} t_p + \kappa_x t'_p & \kappa_y (t_p - t_s)\cot\theta \\ \kappa_y (t_p - t_s)\cot\theta & t_s + \kappa_x t'_s \end{bmatrix} \quad (1)$$

where $t_{p,s}$ is the Fresnel transmission coefficients for p and s waves with $t'_{p,s}$ being the first derivative of $t_{p,s}$ with respect to the incident angle θ. $\kappa_{x,y} = k_{x,y}/k_0$ with $k_{x,y}$ and k_0 being the transverse wavevector and the wavenumber in vacuum, respectively. By adjusting the polarization states before and after the uniaxial

crystal properly, different kinds of spatial differentiations can be realized.

To achieve 2D spatial differentiation, one vortex in the vortex topologic quadrupole should be selected. To this end, the incident polarization state is set as diagonal polarization, that is, $\tilde{\mathbf{E}}_i = \tilde{u}_0(\kappa_x, \kappa_y)[\mathbf{e}_x + \mathbf{e}_y]$ with $\tilde{u}_0$ being the angular spectrum of incident profile. The angular spectrum of the transmitted beam from the uniaxial crystal is $\tilde{\mathbf{E}}_t = \hat{T} \cdot \tilde{\mathbf{E}}_i$. After passing a polarizer whose transmitted axis is identical to the incident polarization, the transmitted angular spectrum becomes

$$\tilde{E}_t = [(t_p + t_s) + \kappa_x(t'_p + t'_s) + \kappa_y(t_p - t_s)\cot\theta]\tilde{u}_0(\kappa_x, \kappa_y) \tag{2}$$

The second and third terms in Equation (2), changing linearly with the transverse wavevector, originate from the angular dispersion of Fresnel coefficients and the geometric Berry phase, respectively. If $t_p = -t_s$, and $t'_p - t'_s$ has a $\pi/2$ phase difference with t_p–t_s, Equation (4) can be reduced as

$$\tilde{E}_t = (t_p - t_s)[\kappa_x\tau + i\kappa_y\cot\theta]\tilde{u}_0(\kappa_x, \kappa_y) \tag{3}$$

where $\tau = i(t'_p - t'_s)/(t_p - t_s)$. Although $|\tau|$ may not equal to $\cot\theta$, the winding order of a close loop in the κ_x–κ_y space is 1.[18] Thus, the uniaxial crystal can be considered a momentum–space modulator, imparting a topologic vortex phase to the incident field. The transmitted field in real space can be obtained via a Fourier transformation:

$$E_t(x, y) = \frac{t_p - t_s}{ik_0}\left[\tau\frac{\partial u_0(x, y)}{\partial x} + i\cot\theta\frac{\partial u_0(x, y)}{\partial y}\right] \tag{4}$$

The outputted light field is the sum of the x- and y-directional spatial differentiations for the given input distribution $u_0(x,y)$. Only if $|\tau|$ and $\cot\theta$ are equal, the coefficients for the x- and y-directional spatial differentiation are identical, which gives isotropic 2D spatial differentiation imaging. If $u_0(x,y)$ is a Gaussian profile, an optical vortex with +1 topologic charge will be generated.

One can find from Equation (1) that, for an x-polarized incident field, the x-component of the transmitted beam is $\tilde{E}_{t,x} = [t_p + \kappa_x t'_p]\tilde{u}_0(\kappa_x, \kappa_y)$. Since $|t_p|$ is close to 1, the transmitted beam is nearly identical to the incident beam, thus can be used for the bright-field imaging. The y-component of the transmitted beam can perform the y-directional spatial differentiation:

$$\tilde{E}_{t,y} = \kappa_y(t_p - t_s)\cot\theta\tilde{u}_0(\kappa_x, \kappa_y) \tag{5}$$

since only the wavevector-varying geometric Berry phase is selected. However, when t_p–t_s tends to zero, we should expand t_p–t_s into Taylor series. Taking the first order approximation, Equation (5) becomes

$$\tilde{E}_{t,y} = \kappa_x\kappa_y(t'_p - t'_s)\cot\theta\tilde{u}_0(\kappa_x, \kappa_y) \tag{6}$$

Equation (6) is valid when the light field is around normal incidence (the incident angle is close to 0). In the real space, the outputted field is the second-order spatial differentiation for the given input distribution: $E_{t,y}(x, y) = (t'_s - t'_p)k_0^2\cot\theta\partial^2 u_0/\partial x\partial y$.[23] Therefore, by adjusting the input and output polarizers, as well as the incident angle of light fields to change the momentum–space modulation function of crystal, the bright-field, 1D, 2D, and second-order spatial differentiation imaging can be flexibly switched.

3. Incoherence Influences on the Momentum–Space Modulation by Uniaxial Crystals

Incoherent light source such as LED is much more suitable for optical imaging than laser sources, since the incoherent light sources can provide more uniform illumination. However, the incoherence of LED sources may make influence to the spatial differentiation effect produced by the uniaxial crystal. To investigate this influence, we study the influence of the incoherence on the optical vortex generation. Assume that the input beam is a Gaussian Schell-model beam, whose cross-spectral density is[25]

$$W^{(0)}(\mathbf{r}_1, \mathbf{r}_2) = \exp\left[-\frac{|\mathbf{r}_1|^2 + |\mathbf{r}_2|^2}{4\sigma_s^2} - \frac{(\mathbf{r}_2 - \mathbf{r}_1)^2}{2\sigma_g^2}\right] \tag{7}$$

with $\mathbf{r}_{1,2} = (x_{1,2}, y_{1,2})$, and $\sigma_{s,g}$ being the widths of the transverse intensity profile and of the degree of coherence, respectively. The degree of global coherence $q = \sigma_g/\sigma_s$ can be used to describe the coherence of Gaussian Schell-model beam. In the limit of $q \to \infty$, the Gaussian Schell-model beam is fully spatially coherent.[26] The 4D Fourier transform of the cross-spectral density can be calculated as

$$\tilde{W}^{(0)}(\mathbf{f}_1, \mathbf{f}_2) = \frac{A^2}{(4\pi)^2(a^2 - b^2)}\exp[-\alpha|\mathbf{f}_1|^2 - \alpha|\mathbf{f}_2|^2 - \beta\mathbf{f}_1 \cdot \mathbf{f}_2] \tag{8}$$

where $\mathbf{f}_{1,2} = (k_0\kappa_{x1,2}, k_0\kappa_{y1,2})$, $\alpha = a/4(a^2 - b^2)$, and $\beta = b/4(a^2 - b^2)$ with $a = 1/4{\sigma_s}^2 + 1/2{\sigma_g}^2$ and $b = 1/2{\sigma_g}^2$. For a diagonal input polarization, the same diagonal polarization component of transmitted beam through a uniaxial crystal can be given by[25,27]

$$\tilde{W}_t(\mathbf{f}_1, \mathbf{f}_2) = (t_p - t_s)^2\tilde{W}^{(0)}(\mathbf{f}_1, \mathbf{f}_2)[\kappa_{x1}\tau + i\kappa_{y1}\cot\theta][\kappa_{x2}\tau^* - i\kappa_{y2}\cot\theta] \tag{9}$$

Therefore, the cross-spectrum of the transmitted beam is

$$W_t(\mathbf{r}_1, \mathbf{r}_2, z_1, z_2) = \int\int \tilde{W}_t(\mathbf{f}_1, \mathbf{f}_2)\exp[\frac{ik_0}{2}(|\mathbf{f}_2|^2 z_2 - |\mathbf{f}_1|^2 z_1) + ik_0(\mathbf{f}_2 \cdot \mathbf{r}_2 - \mathbf{f}_1 \cdot \mathbf{r}_1)]d^2\mathbf{f}_1 d^2\mathbf{f}_2 \tag{10}$$

When $z_1 = z_2 = z$, the cross-spectral density at the z-plane can be calculated as

$$\begin{aligned} W_t(\mathbf{r}_1, \mathbf{r}_2, z) = {} & \frac{(t_p - t_s)^2}{64(a^2 - b^2)k_0^2\eta^3}\exp\left[-\frac{\gamma\mathbf{r}_1^2 + \gamma^*\mathbf{r}_2^2 - 2\beta\mathbf{r}_1 \cdot \mathbf{r}_2}{4\eta}\right] \\ & \times\{|\tau|^2[-2\beta - (\gamma x_1 - \beta x_2)(\gamma^* x_2 - \beta x_1)] \\ & + \cot^2\theta[-2\beta - (\gamma y_1 - \beta y_2)(\gamma^* y_2 - \beta y_1)] \\ & + i[\tau\cot\theta(\gamma x_1 - \beta x_2)(\gamma^* y_2 - \beta y_1) \\ & - \tau^*\cot\theta(\gamma^* x_2 - \beta x_1)(\gamma y_1 - \beta y_2)] \end{aligned} \tag{11}$$

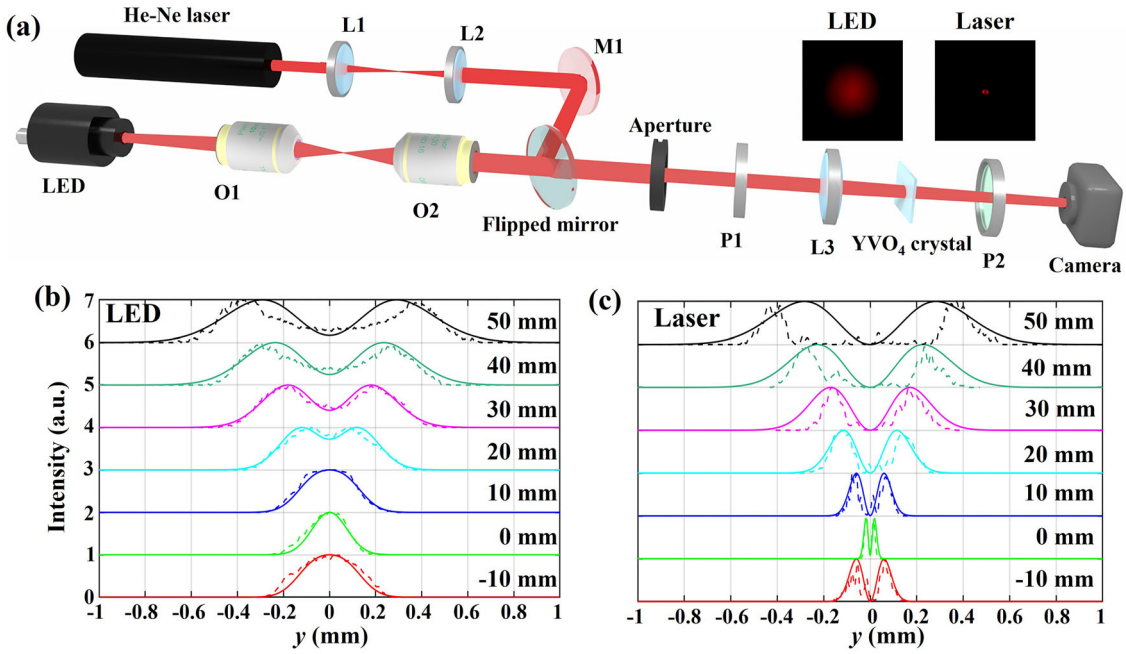

Figure 2. Comparisons of He—Ne laser and red LED sources in the generation of single-charged optical vortex. a) Experiment setup. b,c) Transverse intensity profiles for laser and LED sources changing with the propagation distance, where the solid and dotted lines represent the theoretical and experimental results, respectively. Insets in (a) give the intensity patterns for laser and LED sources in the focal plane.

where $\gamma = \alpha + iz/2k_0$ and $\eta = \gamma\gamma^* - \beta^2$. By setting $\mathbf{r}_1 = \mathbf{r}_2$, we get the intensity distribution at the z-plane.

The comparison of the completely coherent laser source and the partially coherent LED source in the generation of single optical vortex (momentum–space modulation effect of uniaxial crystal) is demonstrated in **Figure 2**. As shown by the experiment setup in Figure 2a, a 632.8 nm He-Ne laser and a red LED source (centered at 635 nm with a bandwidth of 15 nm) are collimated and expanded into large beam sizes (≈4 mm). After combined with a flipped mirror, the laser and LED sources pass through a hard aperture with a diameter of 0.8 mm in order to identify their intensity profiles. Then, the two beams are diagonally polarized by a polarizer P1 and focused into a $10 \times 10 \times 1$ mm YVO_4 crystal ($n_o = 1.9929$, $n_e = 2.2154$, uncoated) via an $f = 50$ mm optical lens. After passing a polarizer P2, a moveable camera is used to record the beam profiles of laser and LED beam alternatively. Comparing the recorded intensity profiles in the focal plane of optical lens (the insets in Figure 2a one finds that, an imperfect, small-size optical vortex emerges in the laser beam, while a large-size bright spot in the LED beam. It indicates that the optical vortex is washed out due to the spatial incoherence of LED source. The intensity distributions for laser and LED beams at different propagation distances z are measured and compared with the theoretical predications of Equation (11). When the degree of global coherence is taken as $q = 0.25$ for the LED beam, the theoretical predications are in good agreement with the experiment results. In the theoretical predications, the laser beam is regarded as a fully spatially coherent Gaussian beam source ($q \to \infty$). The predications do not agree well with the measured results for laser beam owing to the appearance of oscillation wings in the measured profiles. The oscillation wings are caused by the hard aperture, which cuts the light field and arises high spatial frequency components that lead to oscillation wings away from the focal plane ($z > 30$ mm).

As shown in Figure 2b,c, the central dips indicate that the optical vortex always exits in the laser beam, while the optical vortex only appears at the plane away from the focal plane $z = 0$ for the LED beam. The uniaxial crystal can be considered a beam modulator in momentum space. Thus, the modulation effect is independent of the crystal position. And the effect can survive in the far field (both far before and after the focal plane) even for incoherent light beams. Near the focal plane, however, the incoherence of the LED source results in incoherent superposition of momentum–space waves, washing out the modulation effect of the uniaxial crystal. Thus, the optical vortex disappears near the focal plane.

4. Phase-Contrast Microscopy

To build a phase-contrast microscope, the incoherence-induced wash-out effect of the momentum–space modulation should be avoided. To this end, we simply choose Kohler illumination to form an inverted microscope. As shown in **Figure 3**a, a red LED source passes through a collimation system to uniform illumination. The scattering light from sample is collected by an objective and focused into a camera with a lens of $f = 50$ mm. The 1 mm thickness YVO_4 crystal is sandwiched by two polarizers (P1 and P2) to form a phase-contrast module. Without the sample, the illumination light is nearly collimated into the camera with a size of ≈5 mm. Since the CCD is far away from the focal plane, the momentum–space modulation effect of uniaxial crystal is not washed out, thus the spatial differentiation for the imaged objective can be performed.

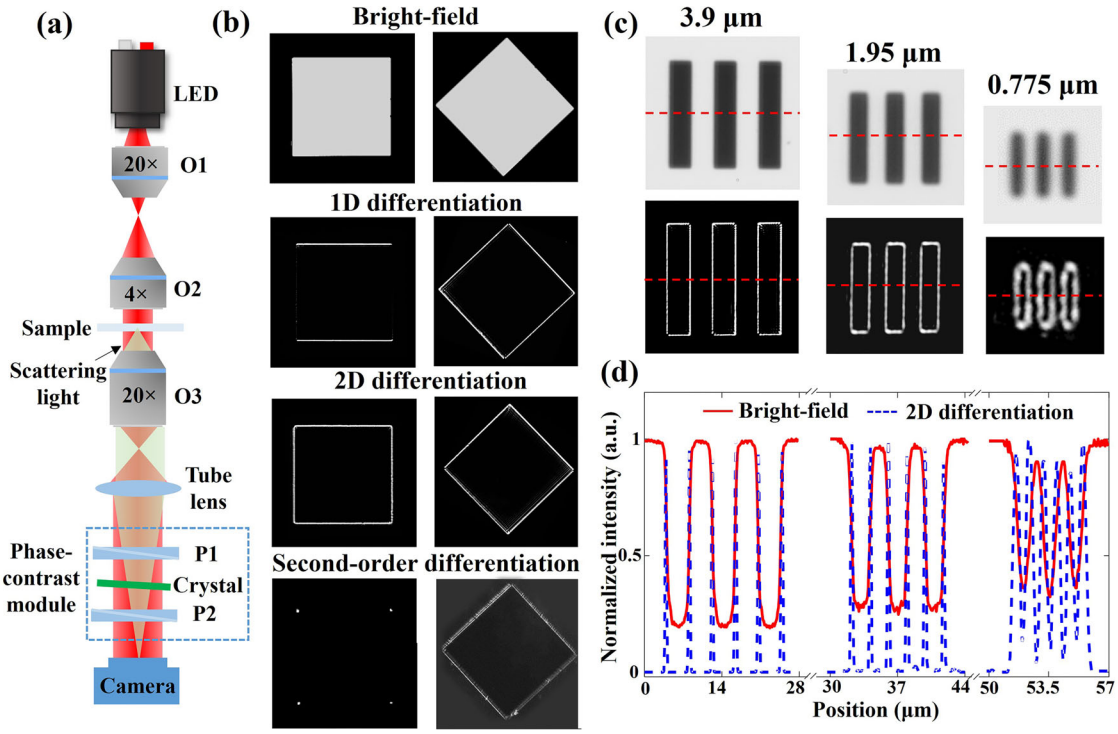

Figure 3. a) Configuration of phase-contrast microscope with a phase-contrast module containing a 1 mm-thickness YVO4 crystal and two rotatable polarizers. b) Bright-field, 1D, 2D, and second-order spatial differentiation imaging for square targets. c) 2D spatial differentiation imaging for vertical line sets with 3.9, 1.95, and 0.775 μm line widths. d) Intensity profiles along the red lines in (c).

Figure 3b gives the comparisons of the bright-field, 1D, 2D, and second-order spatial differentiation imaging for square targets in a negative resolution board (USAF 1951, LBTEK). The YVO4 crystal makes an angle of 4.5° with the z-axis, at which $t_p = -t_s = 0.75i$, $t'_p \approx -t'_s = 230$. When the transmission axes of polarizer P1 and P2 are respectively along the x- and y-axes, namely, $\phi_1 = \phi_2 = 0$, the bright field imaging of the resolution board is captured (see the first row of Figure 3b). By adjusting the transmission axes as $\phi_1 = 0°$ and $\phi_2 = 90°$, the 1D spatial differentiation for square targets is performed. The upper and lower edges of the unrotated square target (the first column in Figure 3b) are detected. For the rotated target (the second column in Figure 3b), however, all edges are detected. When the transmission axes of P1 and P2 are respectively $\phi_1 = 45°$ and $\phi_2 = 45°$, the 2D spatial differentiation for resolution board are conducted. Since the parameter $|\tau|$ is unequal to $\cot\theta$, the 2D spatial differentiation is anisotropic. Although all edges are extracted for both the rotated and unrotated square targets. For the unrotated target, the upper and lower edges are a little brighter than the right and left edges. When the YVO4 crystal is untilted (the incident angle is zero) and the transmission axes of P1 and P2 are orthogonal, the second-order spatial differentiation is conducted according to Equation (6). The four corners of the unrotated square are detected. For the rotated square, however, the four edges are detected. However, the detected edges emerge as double square boxes. It is worth noting that by rotating the phase-contrast module, the derivation directions (the x- and y-axes) for spatial differentiations will be changed accordingly, which allows us to extract the edges and corners along certain directions. One can conclude therefore that various detection tasks can be performed with a simple uniaxial crystal.

To test the spatial resolution of the spatial differentiator, a positive resolution board (USAF 1951, Edmund) is used. With a 50× objective, the vertical line sets with 3.9, 1.95, and 0.775 μm line widths are measured. As shown in Figure 3c,d, the edges of all line sets are extracted. Although there are no obvious flat regions in the bright-field image for the 0.775 μm line sets, the edges are still obtained with fair quality. The contrast of detected edge with respect to the background is defined as the ratio between the peak intensity of edge and average intensity of background. The average contrasts of 6 edges for 3.9, 1.95, and 0.775 μm line sets are estimated as ≈70, ≈42, and ≈12, respectively. Since the uniaxial-crystal-based spatial differentiator is located after the tube lens and makes a spatial differentiation on the light field just before imaged CCD camera, the differentiator makes no influence on the spatial resolution of the imaging system, which depends mainly on the numerical aperture of objective.

In the following, we compare the spatial differentiations for amplitude targets with coherent laser and incoherent LED sources. As shown in **Figure 4**a, the bright field imaging qualities for numbers of "1"–"6" based on laser illumination are much worse than those based on LED illumination. In the laser imaging, the imaging patterns are nonuniform with unsharp pattern edges owing to the laser speckle interference effect. The nonuniformity and unsharpness result in blurry and nonuniform edges in the spatial differentiation patterns, as shown in the second row

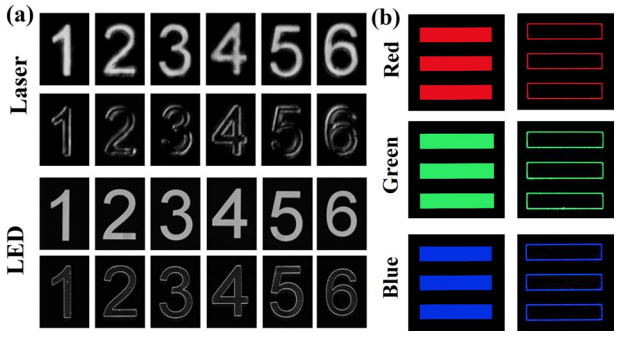

Figure 4. a) Comparisons of He-Ne laser and red LED sources in the spatial differentiation for amplitude targets. The first- and third-rows are bright-field imaging, while the second- and 4th-rows are spatial differentiation imaging. b) Spatial differentiation imaging for horizontal line sets with red, green, and blue LED illuminations.

of Figure 4a. Taking the advantage of the uniform incoherent LED illumination, spatial differentiation patterns in the last row of Figure 4a are not only uniform but also in high contrast.

The broadband property of the spatial differentiations based on uniaxial crystal is examined by red, green, and blue LED sources. Under three source illuminations, all the edges of horizontal line sets are extracted, as shown in Figure 4b. In order to achieve white light illumination, the dispersion compensation is necessary to overcome the dispersion of crystal, which causes that the incident angle for the generation of single vortex phase varies with the operation wavelength. The crystal dispersion could be practically compensated by a proper dispersion prism.

We employ our phase-contrast microscopy to observe biological cells. First, the undyed onion epidermal cells are observed. As shown in **Figure 5**a–c, the cell boundaries possess lower intensity with respect to the background in the bright-field imaging. In the spatial differentiation imaging, the cell boundaries emerge as bright lines. The spatial differentiation improves the contrast between the cell and background from ≈1.2 to ≈22. As expected, the spatial differentiation images reveal more details of cytoderm and make the single cell contour easy to identify, which would greatly benefit the cell morphological observation.

To observe transparent living cells, mouse embryo fibroblast NIH-3T3 cell are grown in a culture dish. The culture dish is placed in the stage of inverted phase-contrast microscope. Owing to the high transparency of the NIH-3T3 living cells, their bright-field imaging is unclear with a very low contrast, as shown in Figure 5d. In the 2D spatial differentiation mode, however, the living cells can be well observed (see Figure 5e). Along the white lines of Figure 5d,e, the cell boundaries are drowned in the noise

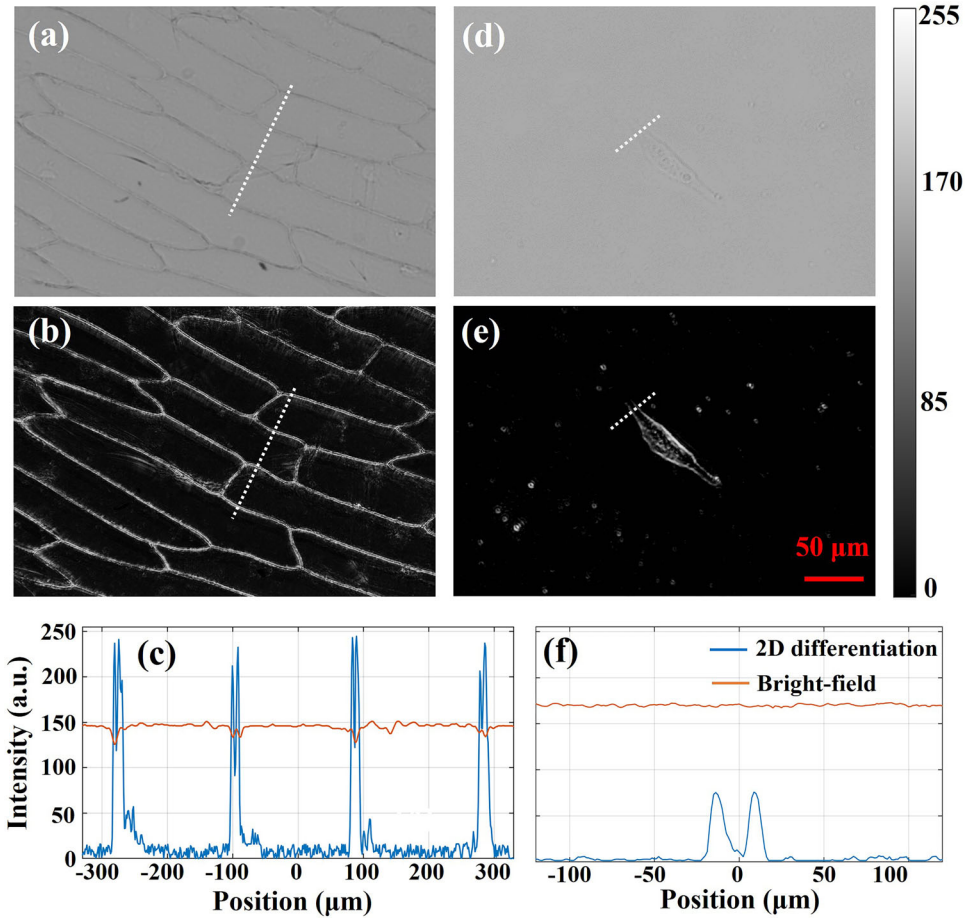

Figure 5. Imaging undyed onion epidermal cells (a–c) and NIH-3T3 living cells (d–f) by the phase-contrast microscope with a 20× objective. a,d) Bright-field imaging, b,e) spatial-differentiation imaging, c,f) Intensity profiles along white lines in (a,b,d,e).

for the bright-field imaging, as shown in Figure 5f. The spatial differentiation imaging, however, provides a high-contrast imaging with a contrast of ≈7, allowing us to identify the transparent NIH-3T3 cell easily.

5. Conclusions

A novel and broadband analog spatial differentiation with incoherent light has been demonstrated based on a versatile uniaxial crystal. The uniaxial crystal can be considered a momentum–space modulator, imparting a topologic vortex phase to the incident field. The momentum–space modulation will be washed out near the focal plane by the incoherence of light. This has been overcome by choosing Kohler illumination, based on which an inverted phase-contrast microscope is built. In this microscope, the 1D, 2D, and second-order analog spatial differentiation imaging, as well as the bright-field imaging can be flexibly switched and the imaging qualities are much better than those with coherent illuminations.[12,13,27] With the inverted phase-contrast microscope, biologically transparent living cells are imaged with high contrast. These findings open a way for analog computing with incoherent light and facilitate the development of versatile, compact, low-cost, and high-performance phase-contrast microscope.

Acknowledgements

M.Z. and X.L. contributed equally to this work. This project has received funding from National Natural Science Foundation of China (12174156, 11604050, 61675092), Natural Science Foundation of Guangdong Province (2021A1515012632, 202102020605, 2020ZDZX3022), Jinan Outstanding Young Scholar Support Program (JNSBYC-2020117, JNSBYC-2020040). The authors thank D. Ma for helpful discussions.

Conflict of Interest

The authors declare no conflict of interest.

Data Availability Statement

The data that support the findings of this study are available from the corresponding author upon reasonable request.

Keywords

geometric Berry phase, incoherence, optical spatial differentiation, phase contrast microscopy, vortex phase

Received: April 6, 2022
Revised: June 19, 2022
Published online:

[1] F. Zangeneh-Nejad, D. L. Sounas, A. Alù, R. Fleury, *Nat. Rev. Mater.* **2021**, *6*, 207.
[2] Y. Wang, J. Fang, T. Zheng, Y. Liang, Q. Hao, E. Wu, M. Yan, K. Huang, H. Zeng, *Laser Photonics Rev.* **2021**, *15*, 2100189.
[3] A. Komar, R. A. Aoni, L. Xu, M. Rahmani, A. E. Miroshnichenko, D. N. Neshev, *ACS Photonics* **2021**, *8*, 864.
[4] J. Zhou, S. Liu, H. Qian, Y. Li, H. Luo, S. Wen, Z. Zhou, G. Guo, B. Shi, Z. Liu, *Sci. Adv.* **2020**, *6*, eabc4385.
[5] T. Zhu, J. Huang, Z. Ruan, *Adv. Photonics* **2020**, *2*, 016001.
[6] X. Qiu, F. Li, W. Zhang, Z. Zhu, L. Chen, *Optica* **2018**, *5*, 208.
[7] F. Zernike, *Science* **1955**, *121*, 345.
[8] M. R. Arnison, K. G. Larkin, C. J. R. Sheppard, N. I. Smith, C. J. Cogswell, *J. Microsc.* **2004**, *214*, 7.
[9] A. Jesacher, S. Fürhapter, S. Bernet, M. Ritsch-Marte, *Phys. Rev. Lett.* **2005**, *94*, 233902.
[10] C.-S. Guo, Y.-J. Han, J.-B. Xu, J. Ding, *Opt. Lett.* **2006**, *31*, 1394.
[11] S. K. Liu, C. Yang, S. L. Liu, Z. Y. Zhou, Y. Li, Y. H. Li, Z. H. Xu, G. C. Guo, B. S. Shi, *Phys. Rev. Appl.* **2019**, *11*, 044013.
[12] P. Huo, C. Zhang, W. Zhu, M. Liu, S. Zhang, S. Zhang, L. Chen, H. J. Lezec, A. Agrawal, Y. Lu, T. Xu, *Nano Lett.* **2020**, *20*, 2791.
[13] Y. Zhou, H. Zheng, I. I. Kravchenko, J. Valentine, *Nat. Photonics* **2020**, *14*, 316.
[14] K. Huang, Y. Wang, J. Fang, W. Kang, Y. Sun, Y. Liang, Q. Hao, M. Yan, H. Zeng, *Photonics Res.* **2021**, *9*, 259.
[15] K. Huang, J. Fang, M. Yan, E. Wu, H. Zeng, *Nat. Commun.* **2022**, *13*, 1077.
[16] T. Zhu, Y. Zhou, Y. Lou, H. Ye, M. Qiu, Z. Ruan, S. Fan, *Nat. Commun.* **2017**, *8*, 15391.
[17] T. Zhu, C. Guo, J. Huang, H. Wang, M. Orenstein, Z. Ruan, S. Fan, *Nat. Commun.* **2021**, *12*, 680.
[18] D. Xu, S. He, J. Zhou, S. Chen, S. Wen, H. Luo, *Opt. Lett.* **2020**, *45*, 6867.
[19] T. Li, Y. Yang, X. Liu, Y. Wu, Y. Zhou, S. Huang, X. Li, H. Huang, *Opt. Lett.* **2020**, *45*, 3681.
[20] J. Zhou, H. Qian, J. Zhao, M. Tang, Q. Wu, M. Lei, H. Luo, S. Wen, S. Chen, Z. Liu, *Natl. Sci. Rev.* **2021**, *8*, nwaa176.
[21] J. Zhou, H. Qian, C. F. Chen, J. Zhao, G. Li, Q. Wu, H. Luo, S. Wen, Z. Liu, *Proc. Natl. Acad. Sci. U. S. A.* **2019**, *166*, 11137.
[22] C. Guo, M. Xiao, M. Minkov, Y. Shi, S. Fan, *Optica* **2018**, *5*, 251.
[23] W. Zhu, H. Zheng, Y. Zhong, J. Yu, Z. Chen, *Phys. Rev. Lett.* **2021**, *126*, 83901.
[24] A. Volyar, V. Shvedov, T. Fadeyeva, A. S. Desyatnikov, D. N. Neshev, W. Krolikowski, Y. S. Kivshar, *Opt. Express* **2006**, *14*, 3724.
[25] M. Leonard, E. Wolf, *Optical Coherence and Quantum Optics*, Cambridge University Press, Cambridge, UK **1995**.
[26] M. R. Foreman, P. Török, *J. Opt. Soc. Am. A* **2009**, *26*, 2470.
[27] Y. Zhou, W. Wu, R. Chen, W. Chen, R. Chen, Y. Ma, *Adv. Opt. Mater.* **2020**, *8*, 1901523.

